Atmospheric Measurement Techniques Discussions

On-orbit radiometric calibration of SWIR bands of TANSO-FTS onboard GOSAT

Y. Yoshida, N. Kikuchi, and T. Yokota

National Institute for Environmental Studies, 16-2 Onogawa, Tsukuba 305-8506, Japan

Correspondence to: Y. Yoshida (yoshida.yukio@nies.go.jp)

4711

Abstract

The Greenhouse gases Observing SATellite (GOSAT) was launched on 23 January 2009 to monitor global distributions of carbon dioxide and methane. The Thermal And Near-infrared Sensor for carbon Observation-Fourier Transform Spectrometer
5 (TANSO-FTS) onboard GOSAT measures short-wavelength infrared (SWIR) spectrum, and its radiometric accuracy directly influences the accuracy of the retrieved greenhouse gas concentrations. From a 2.5-yr retrieval analysis of GOSAT data, we found that the minimum of the mean-squared value of the residuals (the difference between observed and fitted spectra) and the radiance adjustment factor (one of the ancillary
10 parameter to be retrieved with the gas concentrations for adjusting the radiance level between the bands) changed with time, possibly due to inaccurate degradation correction. In this study, the radiometric degradation of TANSO-FTS was evaluated from the on-orbit solar calibration data and modeled as a function of time and wavenumber for each spectral band. The radiometric degradation of TANSO-FTS Band 1 (centered at
15 0.76 μm) after the launch was evaluated to be about 4 to 6 %, varying with wavenumber, whereas the other two bands (Band 2: 1.6 μm and Band 3: 2.0 μm) showed about 1 % degradation and small wavenumber dependency. When we applied the new degradation model in the retrieval analysis, the above-mentioned issues disappeared.

1   Introduction

20 Atmospheric carbon dioxide (CO_2) and methane (CH_4) are well-known anthropogenic greenhouse gases. The global monitoring of these gases from space is expected to improve our knowledge of the global distribution and seasonal cycle of the carbon flux (Rayner and O'Brien, 2001; Chevallier et al., 2007, 2009; Hungershoefer et al., 2010; Takagi et al., 2011).

25 The Greenhouse gases Observing SATellite (GOSAT) was launched on 23 January 2009 to monitor the global distributions of CO_2 and CH_4 from space. It is equipped with

4712

two instruments: the Thermal And Near infrared Sensor for carbon Observation-Fourier Transform Spectrometer (TANSO-FTS) and the Cloud and Aerosol Imager (TANSO-CAI) (Kuze et al., 2009). The TANSO-FTS is the main instrument to observe CO_2 and CH_4. It measures solar light reflected from the Earth's surface in the short wavelength infrared (SWIR) region (centered at 0.76, 1.6, and 2.0 µm; TANSO-FTS Bands 1, 2, and 3, respectively) with two orthogonal linear polarizations, designated "P" and "S", as well as thermal radiation from the Earth's surface and atmosphere in the thermal infrared (TIR) region (5.5 to 14.3 µm; TANSO-FTS Band 4). Column-averaged dry-air mole fractions of CO_2 and CH_4 (XCO_2 and XCH_4) retrieved from SWIR spectra have been released as the GOSAT SWIR Level 2 product (SWIR L2; Yokota et al., 2009, 2011). Other retrieval algorithms have also been developed and applied to the GOSAT SWIR observations (Oshchepkov et al., 2011; Butz et al., 2011; Parker et al., 2011; O'Dell et al., 2012; Crisp et al., 2012; Schepers et al., 2012). One of the major error sources of the retrieved XCO_2 and XCH_4 is the optical path modification due to atmospheric light scattering. The strength of the optical path modification depends not only on the amount of scattering particles but also on the surface reflectance. Therefore, precise radiometric calibration of TANSO-FTS is needed to retrieve accurate XCO_2 and XCH_4.

Currently, most of the GOSAT SWIR retrieval algorithms use the simple degradation model proposed by Kuze at the Japan Aerospace Exploration Agency (JAXA; A. Kuze, personal communication, 2010; Fig. 1). However, this degradation model has been shown to produce large deviations (Kuze et al., 2011, 2012). Further, the degradation of each band is modeled as a function of time, but the model does not take the polarization and wavenumber dependencies into account. From an analysis of 2.5 yr of retrievals using SWIR L2 version 01.xx (Yoshida et al., 2011), we found two time-dependent issues (see next section for details), which may be related to the degradation model. In this study, we re-evaluated the TANSO-FTS degradation using the on-orbit solar calibration data (i.e., the spectral radiances) and clarified the wavenumber and polarization dependencies more precisely.

2   Time-dependent issues found in the SWIR L2 version 01.xx retrieval

The following two issues were found in the SWIR L2 version 01.xx retrieval results.

ISSUE-1: the minimum of the mean-squared value of the residual of TANSO-FTS Band 1 increased with time (Fig. 2a), probably owing to the changes in the baseline shape of the residual spectrum (Fig. 2b).

ISSUE-2: the ratio between the radiance adjustment factors (see below for definition) changed with time (Fig. 2c).

Both issues were seen only for the ocean cases. In the SWIR L2 version 01.xx retrieval, the handling of the surface reflectance was different for land and ocean cases (Yoshida et al., 2011). Rough spectra of ground surface albedo in each band were retrieved for the land case, whereas the surface wind speed and radiance adjustment factor were retrieved for the ocean case. A water surface reflectance was calculated based on the slope probability distribution function proposed by Cox and Munk (1954). This assumption provides the water surface reflectance over the entire spectral range with a single parameter of surface wind speed. Because the SWIR L2 version 01.xx retrieval utilizes both Band 1 and 2 spectra, one surface wind speed parameter cannot represent the reflectance levels of the entire TANSO-FTS spectral range if the relative accuracy of the degradation between these bands is inaccurate. The radiance adjustment factor adjusts the radiance level between the bands to avoid a retrieval failure. ISSUE-1 can be explained if the Band 1 degradation has a wavenumber dependency, and ISSUE-2 is directly related to the accuracy of the degradation.

3   On-orbit solar calibration

The solar radiation reflected by the onboard Spectralon diffuser plate is introduced into the TANSO-FTS when the satellite passes over the northern polar region. Around 35 ~ 50 scans (about 3 ~ 4 min converted into the data acquisition time) of solar calibration

data were obtained for each orbit (Fig. 3). Both sides of the diffuser plate are used for the solar calibration; the front side is usually exposed to direct solar radiation and the back side is exposed only once a month (Kuze et al., 2011).

In this study, we used the solar calibration data taken with the back side diffuser plate, because it is expected to have suffered less degradation than the front side diffuser (Kuze et al., 2012). Table 1 summarizes the solar calibration data observed by the back side diffuser plate. Furthermore, to discard the data that were contaminated by weak absorption of the terrestrial atmosphere, we selected the solar calibration data with the following criterion. We used the sun-earth-satellite angle θ_{SES} (see Fig. 3) to specify the scan from a series obtained in a single solar calibration. To discover the fine absorption structure, the observed solar spectra were averaged over certain θ_{SES} regions and then their differences were checked (Fig. 4). The absorption structure due to terrestrial atmospheric oxygen can be seen when θ_{SES} is smaller than about 105 degrees. By also considering the data availability (see the range of θ_{SES} in Table 1), we used the data with θ_{SES} just above 105 degrees for each solar calibration in the following analysis.

The general formula of the spectrum observed by TANSO-FTS was a function of the pointing mirror direction. It was expressed as a sum of several Mueller matrices (Eqs. 9 and 10 of Kuze et al., 2012). The pointing mirror pointed the diffuser plate and did not move during the solar calibration, and the incident solar irradiance was regarded as non-polarized light. Therefore, the observed spectrum S of the solar calibration can be expressed as

$$S_{P/S}(v, \theta, \varphi, t) = \frac{F_{SUN}(v)\cos\theta}{\pi R(t)^2} r_{P/S}(v, \theta, \varphi) \, OPT_{P/S}(v) \, A_{P/S}(v, t), \tag{1}$$

where v is a wavenumber; θ and φ are the incident and relative azimuth angles of the incident solar radiation to the diffuser plate, respectively; t is a day after the launch; F_{SUN} is the solar irradiance; R is the distance between Sun and Earth in astronomical units; r is the reflectance of the diffuser plate; OPT is the optical efficiency of the

4715

pointing mirror, TANSO-FTS-mechanism, and after-optics; A is the radiometric degradation of TANSO-FTS; and subscripts "P" and "S" indicate the polarization components.

4 Evaluation of the radiometric degradation of TANSO-FTS

4.1 Incident angle dependency of the diffuser plate

Figure 5a shows the relationship between θ and φ for the solar calibration data observed by the back-side diffuser plate. Each curve corresponds to a single solar calibration. Because the requirement $\theta_{SES} \approx 105$ deg. determines the relationship between θ and φ uniquely, φ is omitted hereafter. To obtain the θ dependency of the diffuser plate reflectance, a special solar calibration was conducted on 4 March 2009 by rotating the whole satellite (corresponding to the three uppermost data in Table 1 and three longest curves in Fig. 5a; Kuze et al., 2012). In this case, Eq. (1) can be written as

$$\frac{S_{P/S}(v, \theta, t)}{r_{P/S}(v, \theta)\cos\theta} = \frac{F_{SUN}(v)}{\pi R(t)^2} OPT_{P/S}(v) \, A_{P/S}(v, t) = const \tag{2}$$

Therefore, the diffuser plate reflectance normalized by the reference reflectance observed at θ_0 becomes

$$\frac{r_{P/S}(v, \theta)}{r_{P/S}(v, \theta_0)} = \frac{\cos\theta_0}{\cos\theta} \frac{S_{P/S}(v, \theta, t)}{S_{P/S}(v, \theta_0, t)}. \tag{3}$$

In this study, the uppermost data in Table 1 was selected as the reference spectrum; i.e., $\theta_0 = 33$ degree. If the diffuser plate is Lambertian, Eq. (3) becomes unity; however, it showed clear θ dependency (Fig. 6). In addition, the degree of θ dependency varied with wavenumber and polarization. To make a diffuser plate reflectance model, the observed spectrum was first fitted by a cubic-spline curve. Then, the θ dependency was evaluated at each wavenumber point. The diffuser plate reflectance was assumed to

4716

be expressed as a second-order polynomial of $\cos\theta$, although the validity of this assumption could not be confirmed because of the insufficient number of incident angles.

$$\frac{r_{P/S}(v,\theta)}{r_{P/S}(v,\theta_0)} \approx a_{P/S}(v)\cos^2\theta + b_{P/S}(v)\cos\theta + c_{P/S}(v). \tag{4}$$

The evaluated coefficients a, b, and c are summarized in Table 2.

4.2 Radiometric degradation of TANSO-FTS

From Eq. (1), the relative degradation of TANSO-FTS can be written as

$$\frac{A_{P/S}(v,t)}{A_{P/S}(v,t_0)} = \frac{R(t)^2}{R(t_0)^2} \frac{\cos\theta_0}{\cos\theta} \frac{S_{P/S}(v,\theta,t)}{S_{P/S}(v,\theta_0,t_0)} \frac{r_{P/S}(v,\theta_0)}{r_{P/S}(v,\theta)}$$
$$\approx \frac{R(t)^2}{R(t_0)^2} \frac{\cos\theta_0}{\cos\theta} \frac{S_{P/S}(v,\theta,t)}{S_{P/S}(v,\theta_0,t_0)} \frac{1}{a_{P/S}(v)\cos^2\theta + b_{P/S}(v)\cos\theta + c_{P/S}(v)} \tag{5}$$

The reference spectrum is the same as that in previous section; i.e., $t_0 = 40$ (4 March 2009) and $\theta_0 = 33$ degree. By performing a similar fitting process to that in the previous section, we evaluated the radiometric degradations of TANSO-FTS at specific wavenumbers (Fig. 7). These results are roughly consistent with those of Kuze et al. (2012). However, we obtained several new findings because they did not consider the wavenumber and polarization dependencies.

The sensitivity degraded exponentially for all bands except in the higher wavenumber region ($> 5050\,\text{cm}^{-1}$) of Band 3P. The reason for this unexpected sensitivity increase was unclear. Among the GOSAT SWIR retrievals (Yoshida et al., 2011; Oshchepkov et al., 2011; Butz et al., 2011; Parker et al., 2011; Crisp et al., 2012; Schepers et al., 2012), none were used in this wavenumber region for greenhouse gas retrieval, although Yoshida et al. (2011) and Schepers et al. (2012) used the region for cirrus screening. Because both cirrus screening methods utilize the relationship between the

4717

observed signal level at this wavenumber region and the noise level, the priority of accurate radiometric calibration in this spectral range is not so high. Therefore, we do not discuss this Band 3P issue further in this paper.

The difference in degradation within the band was largest for Band 1 ($\sim 2\%$) and relatively small for Band 2 and 3S ($< 0.5\%$). For Band 1, the degradation of the higher wavenumber region ($> 13\,150\,\text{cm}^{-1}$) was smaller than that of other wavenumber regions. Because the wavenumber-independent degradation correction was applied in the SWIR L2 version 01.xx retrieval, the observed Band 1 spectrum in this wavenumber region suffered excess degradation correction; i.e., the corrected spectrum showed a higher radiance level than the true level and the residual spectrum was expected to have positive value. This tendency coincided with ISSUE-1 (Fig. 2b). Although the actual time constants of degradation for all bands looked similar (Fig. 7), the time constant of Band 1 used in the SWIR L2 version 01.xx retrieval was one-fifth that of Bands 2 and 3 (Fig. 1). To compensate this difference, the ratio of the retrieved radiance adjustment factor could be considered to change with time (ISSUE-2; Fig. 2c).

The degradation for each wavenumber point and polarization was modeled as

$$\frac{A_{P/S}(v,t)}{A_{P/S}(v,t_0)} = d_{P/S}(v) + e_{P/S}(v)\exp\left[-f_{P/S}(v)\cdot t\right] \tag{6}$$

There were several periods that showed slightly large deviation from the exponential form (Fig. 7). These periods corresponded to large incident angle θ, perhaps owing to the assumption of a second-order polynomial for the modeled θ dependency of the diffuser plate reflectance (Eq. 4). Here, data with θ larger than 35 degree were not used when the coefficients d, e, and f were evaluated. The evaluated coefficients are summarized in Table 3. Figure 8 shows the TANSO-FTS degradation over 5.5 yr (the lifetime of GOSAT was designed to be 5 yr) calculated from the evaluated degradation model in this study.

4718

4.3 Retrieval test using the evaluated degradation model

We performed a retrieval test using the evaluated degradation model. For the absolute value of the TANSO-FTS degradation, we used the vicarious calibration campaign results (Table IV of Kuze et al., 2011). Here, we focus on whether the time-dependent issues were solved or not. We do not discuss the retrieved XCO_2 and XCH_4 values because this subject is beyond of the scope of this paper, and the impact of the degradation correction on the retrieved XCO_2 and XCH_4 depends on the retrieval setting. Figure 9 shows the updated retrieval results. Both the minimum of the mean-squared value of the Band 1 residual and the ratio between the radiance adjustment factors flattened in time, and the Band 1 residual spectra for different years showed a similar baseline shape. Therefore, the root cause of the time-dependent issues in the SWIR L2 version 01.xx was concluded to be the accuracy of the degradation model.

5 Conclusions

The radiometric degradation of TANSO-FTS was evaluated from the on-orbit solar calibration data. The radiometric sensitivity degraded exponentially for all bands except for the higher wavenumber region of Band 3P, and the time constant of degradation depended on the wavenumber and polarization. Band 1 showed the largest degradation (about 6 % at the end of 2011) and had the largest wavenumber dependency within the bands. A new degradation model was constructed from the evaluated results. The predicted degradation after 2012 from this new degradation model is expected to be smaller than 1 % for all bands. By applying the new degradation model to the retrieval, we eliminated the time-dependent issues seen in the SWIR L2 version 01.xx retrieval. The new degradation model is expected to suppress a possible time-dependent bias error in the retrieval results.

References

Butz, A., Guerlet, S., Hasekamp, O., Schepers, D., Galli, A., Aben, I., Frankenberg, C., Hartmann, J.-M., Tran, H., Kuze, A., Keppel-Aleks, G., Toon, G., Wunch, D., Wennberg, P., Deutscher, N., Griffith, D., Macatangay, R., Messerschmidt, J., Notholt, J., and Warneke, T.: Toward accurate CO_2 and CH_4 observations from GOSAT, Geophys. Res. Lett., 38, L14812, doi:10.1029/2011GL047888, 2011.

Chevallier, F., Bréon, F.-M., and Rayner, P. J.: Contribution of the orbiting carbon observatory to the estimation of CO_2 sources and sinks: theoretical study in a variational data assimilation framework, J. Geophys. Res., 112, D09307, doi:10.1029/2006JD007375, 2007.

Chevallier, F., Maksyutov, S., Bousquet, P., Bréon, F.-M., Saito, R., Yoshida, Y., and Yokota, T.: On the accuracy of the CO_2 surface fluxes to be estimated from the GOSAT observations, Geophys. Res. Lett., 36, L19807, doi:10.1029/2009GL040108, 2009.

Cox, C. and Munk, W.: Measurement of the roughness of the sea surface from photographs of the Sun's glitter, J. Opt. Soc. Am., 44, 838–850, 1954.

Crisp, D., Fisher, B. M., O'Dell, C., Frankenberg, C., Basilio, R., Bösch, H., Brown, L. R., Castano, R., Connor, B., Deutscher, N. M., Eldering, A., Griffith, D., Gunson, M., Kuze, A., Mandrake, L., McDuffie, J., Messerschmidt, J., Miller, C. E., Morino, I., Natraj, V., Notholt, J., O'Brien, D. M., Oyafuso, F., Polonsky, I., Robinson, J., Salawitch, R., Sherlock, V., Smyth, M., Suto, H., Taylor, T. E., Thompson, D. R., Wennberg, P. O., Wunch, D., and Yung, Y. L.: The ACOS CO_2 retrieval algorithm – Part II: Global XCO_2 data characterization, Atmos. Meas. Tech., 5, 687–707, doi:10.5194/amt-5-687-2012, 2012.

Hungershoefer, K., Breon, F.-M., Peylin, P., Chevallier, F., Rayner, P., Klonecki, A., Houweling, S., and Marshall, J.: Evaluation of various observing systems for the global monitoring of CO_2 surface fluxes, Atmos. Chem. Phys., 10, 10503–10520, doi:10.5194/acp-10-10503-2010, 2010.

Kuze, A., Suto, H., Nakajima, M., and Hamazaki, T.: Thermal and near infrared sensor for carbon observation Fourier-transform spectrometer on the greenhouse gases observing satellite for greenhouse gases monitoring, Appl. Optics, 48, 6716–6733, 2009.

Kuze, A., O'Brien, D. M., Taylor, T. E., Day, J. O., O'Dell, C. W., Kataoka, F., Yoshida, M., Mitomi, Y., Bruegge, C. J., Pollock, H., Basilio, R., Helmlinger, M., Matsunaga, T., Kawakami, S., Shiomi, K., Urabe, T., and Suto, H.: Vicarious calibration of the GOSAT sensors using the railroad valley desert playa, IEEE T. Geosci. Remote, 49, 1781–1795, doi:10.1109/TGRS.2010.2089527, 2011.

Kuze, A., Suto, H., Shiomi, K., Urabe, T., Nakajima, M., Yoshida, J., Kawashima, T., Yamamoto, Y., and Kataoka, F.: Level 1 algorithms for TANSO on GOSAT: processing and on-orbit calibrations, Atmos. Meas. Tech. Discuss., 5, 2959–3018, doi:10.5194/amtd-5-2959-2012, 2012.

O'Dell, C. W., Connor, B., Bösch, H., O'Brien, D., Frankenberg, C., Castano, R., Christi, M., Crisp, D., Eldering, A., Fisher, B., Gunson, M., McDuffie, J., Miller, C. E., Natraj, V., Oyafuso, F., Polonsky, I., Smyth, M., Taylor, T., Toon, G. C., Wennberg, P. O., and Wunch, D.: Corrigendum to "The ACOS CO_2 retrieval algorithm – Part 1: Description and validation against synthetic observations" published in Atmos. Meas. Tech., 5, 99–121, 2012, Atmos. Meas. Tech., 5, 193–193, doi:10.5194/amt-5-193-2012, 2012.

Oshchepkov, S., Bril, A., Maksyutov, S., and Yokota, T.: Detection of optical path in spectroscopic space-based observations of greenhouse gases: application to GOSAT data processing, J. Geophys. Res., 116, D14304, doi:10.1029/2010JD015352, 2011.

Parker, R., Boesch, H., Cogan, A., Fraser, A., Feng, L., Palmer, P. I., Messerschmidt, J. Deutscher, N., Griffith, D. W. T., Notholt, J., Wennberg, P. O., Wunch, D.: Methane observations from the greenhouse gases observing satellite: comparison to ground-based TCCON data and model calculations, Geophys. Res. Lett., 38, L15807, doi:10.1029/2011GL047871, 2011.

Rayner, P. J. and O'Brien, D. M.: The utility of remotely sensed CO_2 concentration data in surface source inversions, Geophys. Res. Lett., 28, 175–178, 2001.

Schepers, D., Guerlet, S., Butz, A., Landgraf, J., Frankenberg, C., Hasekamp, O., Blavier, J.-F., Deutscher, N. M., Griffith, D. W. T., Hase, F., Kyro, E., Morino, I., Sherlock, V., Sussmann, R., and Aben, I.: Methane retrievals from greenhouse gases observing satellite (GOSAT) shortwave infrared measurements: performance comparison of proxy and physics retrieval algorithms, J. Geophys. Res., 117, D10307, doi:10.1029/2012JD017549, 2012.

Takagi, H., Saeki, T., Oda, T., Saito, M., Valsala, V., Belikov, D., Saito, R., Yoshida, Y., Morino, I., Uchino, O., Andres, R. J., Yokota, T., and Maksyutov, S.: On the benefit of GOSAT observations to the estimation of regional CO_2 fluxes, Scientific Online Letters on the Atmosphere, 7, 161–164, doi:10.2151/sola.2011-041, 2011.

Yokota, T., Yoshida, Y., Eguchi, N., Ota, Y., Tanaka, T., Watanabe, H., and Maksyutov, S.: Global concentrations of CO_2 and CH_4 retrieved from GOSAT: first preliminary results, SOLA, 5, 160–163, doi:10.2151/sola.2009-041, 2009.

Yoshida, Y., Ota, Y., Eguchi, N., Kikuchi, N., Nobuta, K., Tran, H., Morino, I., and Yokota, T.: Retrieval algorithm for CO_2 and CH_4 column abundances from short-wavelength infrared spectral observations by the Greenhouse gases observing satellite, Atmos. Meas. Tech., 4, 717–734, doi:10.5194/amt-4-717-2011, 2011.

Table 1. On-orbit solar calibration data observing with the back-side diffuser plate. On 30 July 2009, the data suitable for the analysis was not available.

DD/MM/YYYY hh:mm ~ hh:mm	Day after launch	Range of θ_{SES} [deg.]	θ [deg.] ($\theta_{SES} \approx 105$)
04/03/2009 13 : 51 ~ 13 : 59	40	122.1 ~ 95.6	33.0
04/03/2009 15 : 30 ~ 15 : 37	40	122.1 ~ 95.6	41.1
04/03/2009 18 : 46 ~ 18 : 53	40	122.0 ~ 95.6	26.2
29/04/2009 03 : 28 ~ 03 : 32	96	105.6 ~ 91.9	32.0
28/06/2009 03 : 25 ~ 03 : 29	156	105.9 ~ 92.1	32.3
01/07/2009 03 : 25 ~ 03 : 29	159	105.8 ~ 92.0	32.5
30/07/2009 22 : 32 ~ 22 : 35	188	104.7 ~ 91.9	N/A
29/08/2009 22 : 34 ~ 22 : 38	218	105.8 ~ 91.9	33.7
28/09/2009 22 : 37 ~ 22 : 41	248	105.9 ~ 92.1	33.4
28/10/2009 22 : 40 ~ 22 : 44	278	105.9 ~ 92.1	34.4
27/11/2009 22 : 42 ~ 22 : 46	308	106.1 ~ 92.1	37.3
27/12/2009 22 : 43 ~ 22 : 46	338	106.2 ~ 92.1	40.7
26/01/2010 22 : 41 ~ 22 : 45	368	106.0 ~ 91.9	42.0
25/02/2010 22 : 38 ~ 22 : 42	398	106.1 ~ 92.0	39.9
27/03/2010 22 : 35 ~ 22 : 39	428	107.1 ~ 93.1	35.8
26/04/2010 22 : 32 ~ 22 : 36	458	107.0 ~ 93.2	32.4
26/05/2010 22 : 30 ~ 22 : 34	488	105.5 ~ 91.8	31.4
25/06/2010 22 : 30 ~ 22 : 34	518	106.3 ~ 92.0	32.3
25/07/2010 22 : 31 ~ 22 : 35	548	106.4 ~ 92.6	33.5
27/08/2010 22 : 33 ~ 22 : 37	581	108.1 ~ 94.3	33.6
26/09/2010 22 : 37 ~ 22 : 41	611	105.8 ~ 92.1	33.3
26/10/2010 22 : 41 ~ 22 : 45	641	106.1 ~ 92.4	34.1
25/11/2010 22 : 43 ~ 22 : 47	671	105.9 ~ 92.1	36.8
25/12/2010 22 : 44 ~ 22 : 47	701	107.6 ~ 97.3	40.2
24/01/2011 22 : 43 ~ 22 : 45	731	108.0 ~ 97.6	41.7
23/02/2011 22 : 41 ~ 22 : 44	761	105.9 ~ 95.6	39.7
25/03/2011 22 : 38 ~ 22 : 41	791	107.3 ~ 97.1	35.6
27/04/2011 22 : 35 ~ 22 : 38	824	105.6 ~ 95.5	31.7
27/05/2011 22 : 33 ~ 22 : 36	854	107.7 ~ 97.7	30.7
26/06/2011 22 : 33 ~ 22 : 36	884	105.8 ~ 95.7	31.7
25/08/2011 22 : 37 ~ 22 : 40	944	105.6 ~ 95.5	32.9
27/09/2011 22 : 40 ~ 22 : 43	977	106.4 ~ 96.3	32.6
27/10/2011 22 : 43 ~ 22 : 45	1007	107.8 ~ 97.7	33.6
26/11/2011 22 : 45 ~ 22 : 48	1037	105.8 ~ 95.6	36.5

Table 2. Coefficients a, b, and c of (a) Band 1, (b) 2, and (c) 3 to represent the reflectance of the diffuser plate.

Wavenumber (cm^{-1})	P-polarization			S-polarization		
	a	b	c	a	b	c
(a)						
12 850	−1.013	1.411	0.529	−0.714	0.994	0.668
12 950	0.119	−0.451	1.294	0.020	−0.197	1.151
13 050	0.102	−0.418	1.279	0.076	−0.292	1.192
13 150	−0.173	0.040	1.080	−0.087	−0.008	1.068
13 250	0.830	−1.602	1.760	1.092	−1.950	1.868
(b)						
5750	−0.004	−0.325	1.276	−0.207	0.138	1.023
5850	0.121	−0.526	1.356	0.187	−0.507	1.294
5950	0.098	−0.487	1.339	0.091	−0.346	1.226
6050	0.038	−0.389	1.299	0.070	−0.313	1.213
6150	0.076	−0.449	1.323	0.084	−0.341	1.227
6250	0.109	−0.507	1.348	0.076	−0.327	1.221
6350	0.080	−0.457	1.327	0.106	−0.378	1.243
6450	0.328	−0.865	1.495	0.275	−0.664	1.363
(c)						
4750	−0.092	−0.234	1.252	−0.244	0.191	1.012
4850	−0.090	−0.223	1.250	0.113	−0.409	1.264
4950	−0.029	−0.323	1.291	0.148	−0.457	1.279
5050	−0.103	−0.185	1.228	0.062	−0.314	1.220
5150	−0.211	−0.004	1.152	−0.178	0.088	1.052
5250	−0.296	0.139	1.091	−0.025	−0.173	1.162

Table 3. Coefficients d, e, and f of (a) Band 1, (b) 2, and (c) 3 to represent the radiometric degradation of TANSO-FTS.

Wavenumber	P-polarization			S-polarization		
(cm^{-1})	d	e	f	d	e	f
(a)						
12850	0.940	6.12×10^{-2}	3.85×10^{-3}	0.938	6.48×10^{-2}	3.56×10^{-3}
12900	0.943	5.91×10^{-2}	3.78×10^{-3}	0.937	6.41×10^{-2}	3.18×10^{-3}
12950	0.945	5.69×10^{-2}	3.84×10^{-3}	0.939	6.22×10^{-2}	3.19×10^{-3}
13000	0.934	6.61×10^{-2}	3.32×10^{-3}	0.929	7.04×10^{-2}	2.86×10^{-3}
13050	0.940	6.23×10^{-2}	3.61×10^{-3}	0.934	6.73×10^{-2}	2.98×10^{-3}
13100	0.940	6.29×10^{-2}	3.73×10^{-3}	0.934	6.93×10^{-2}	3.09×10^{-3}
13150	0.943	5.75×10^{-2}	3.44×10^{-3}	0.934	6.47×10^{-2}	2.97×10^{-3}
13200	0.963	3.74×10^{-2}	4.09×10^{-3}	0.953	4.76×10^{-2}	3.15×10^{-3}
13250	0.965	3.80×10^{-2}	5.15×10^{-3}	0.957	4.54×10^{-2}	3.45×10^{-3}
(b)						
5750	0.987	1.52×10^{-2}	4.53×10^{-3}	0.988	1.37×10^{-2}	4.78×10^{-3}
5800	0.987	1.42×10^{-2}	3.65×10^{-3}	0.990	1.15×10^{-2}	4.57×10^{-3}
5850	0.986	1.48×10^{-2}	3.78×10^{-3}	0.988	1.19×10^{-2}	3.71×10^{-3}
5900	0.985	1.51×10^{-2}	3.64×10^{-3}	0.988	1.23×10^{-2}	3.92×10^{-3}
5950	0.986	1.40×10^{-2}	3.66×10^{-3}	0.988	1.19×10^{-2}	3.58×10^{-3}
6000	0.985	1.43×10^{-2}	2.91×10^{-3}	0.987	1.26×10^{-2}	3.61×10^{-3}
6050	0.986	1.43×10^{-2}	3.21×10^{-3}	0.987	1.31×10^{-2}	3.59×10^{-3}
6100	0.986	1.41×10^{-2}	3.35×10^{-3}	0.987	1.25×10^{-2}	2.93×10^{-3}
6150	0.987	1.40×10^{-2}	4.05×10^{-3}	0.987	1.30×10^{-2}	4.02×10^{-3}
6200	0.985	1.42×10^{-2}	2.64×10^{-3}	0.987	1.31×10^{-2}	3.30×10^{-3}
6250	0.985	1.57×10^{-2}	3.00×10^{-3}	0.986	1.46×10^{-2}	3.13×10^{-3}
6300	0.986	1.39×10^{-2}	3.40×10^{-3}	0.987	1.25×10^{-2}	3.17×10^{-3}
6350	0.984	1.67×10^{-2}	3.27×10^{-3}	0.986	1.43×10^{-2}	3.42×10^{-3}
6400	0.983	1.78×10^{-2}	3.51×10^{-3}	0.986	1.50×10^{-2}	3.78×10^{-3}
6450	0.982	2.01×10^{-2}	3.68×10^{-3}	0.985	1.69×10^{-2}	4.95×10^{-3}
(c)						
4750	0.991	1.02×10^{-2}	5.88×10^{-3}	0.985	1.53×10^{-2}	3.56×10^{-3}
4800	0.996	4.06×10^{-3}	3.86×10^{-3}	0.990	1.10×10^{-2}	3.33×10^{-3}
4850	0.997	5.59×10^{-3}	1.54×10^{-2}	0.990	1.07×10^{-2}	2.89×10^{-3}
4900	0.996	5.96×10^{-3}	1.22×10^{-2}	0.990	1.02×10^{-2}	3.84×10^{-3}
4950	0.993	9.84×10^{-3}	7.76×10^{-3}	0.990	1.05×10^{-2}	3.67×10^{-3}
5000	0.994	7.13×10^{-3}	5.04×10^{-3}	0.990	1.07×10^{-2}	3.95×10^{-3}
5050	0.999	-9.53×10^{-6}	9.87×10^{-4}	0.990	1.13×10^{-2}	4.75×10^{-3}
5100	1.007	-8.80×10^{-3}	1.16×10^{-3}	0.989	1.13×10^{-2}	2.90×10^{-3}
5150	1.016	-1.78×10^{-2}	4.61×10^{-4}	0.988	1.22×10^{-2}	4.48×10^{-3}
5200	1.009	-9.13×10^{-3}	1.87×10^{-3}	0.988	1.26×10^{-2}	4.13×10^{-3}
5250	1.043	-5.46×10^{-2}	5.68×10^{-3}	0.976	3.11×10^{-2}	7.37×10^{-3}
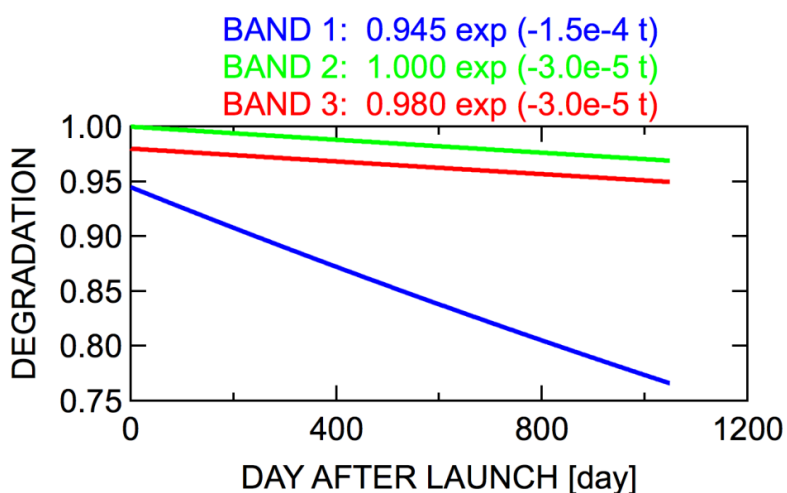
Fig. 1. TANSO-FTS degradation model used in the SWIR L2 version 01.xx retrieval analysis.
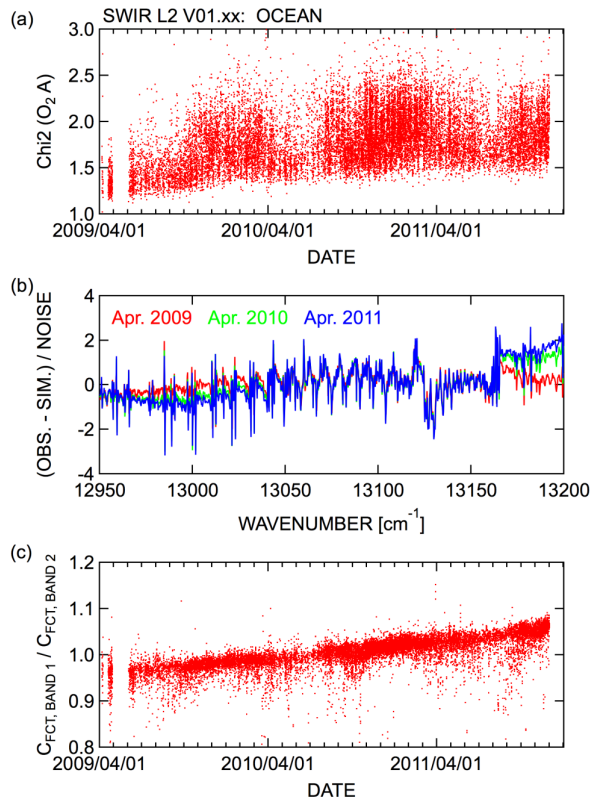
Fig. 2. Time-dependent issues found in the SWIR L2 version 01.xx retrieval. **(a)** Mean-squared value of the TANSO-FTS Band 1 residuals, **(b)** residual spectra of TANSO-FTS Band 1 for different years, and **(c)** ratio between the retrieved radiance adjustment factors.
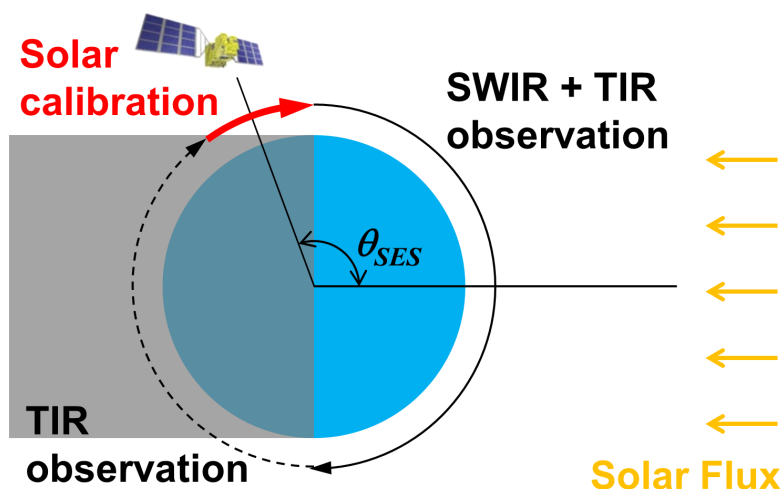
4727

Fig. 3. On-orbit operation of GOSAT. Solar calibration is conducted when the satellite passes over the northern polar region.
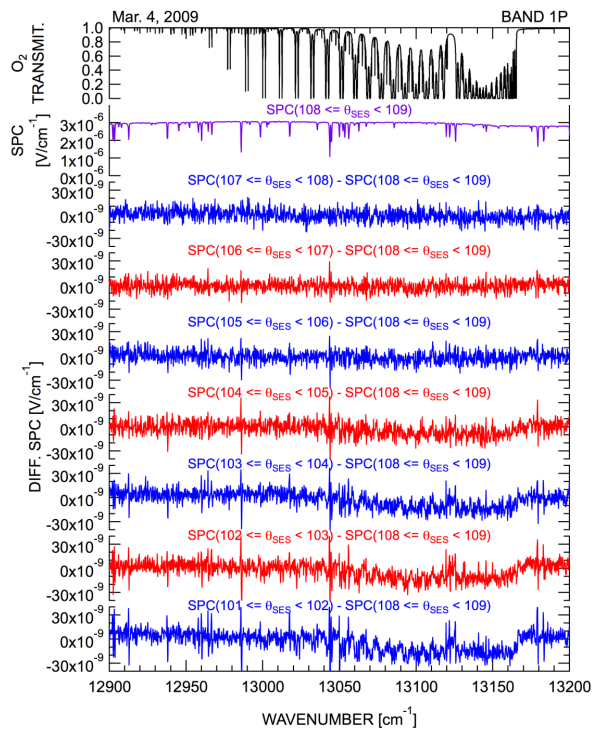
Fig. 4. An example of the averaged solar spectrum over the specified θ_{SES} range (purple) and their differences (red and blue). As for the reference, transmittance of the terrestrial atmospheric oxygen (black) is also shown.

4729
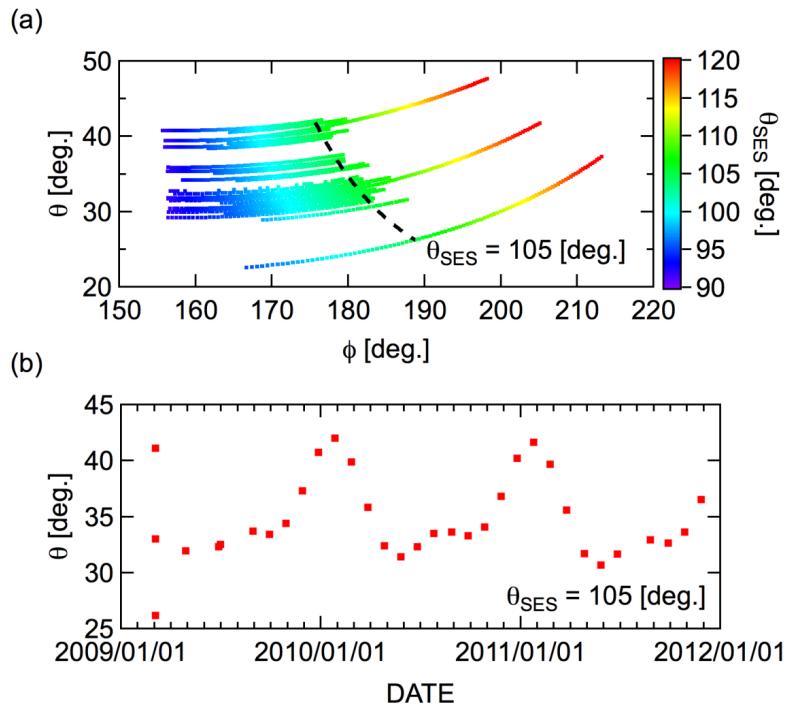
Fig. 5. (a) Relationship between the incident angle and relative azimuth angle of solar radiation to the diffuser plate. **(b)** The incident angle of solar radiation to the diffuser plate for $\theta_{SES} \approx 105$ degree cases.
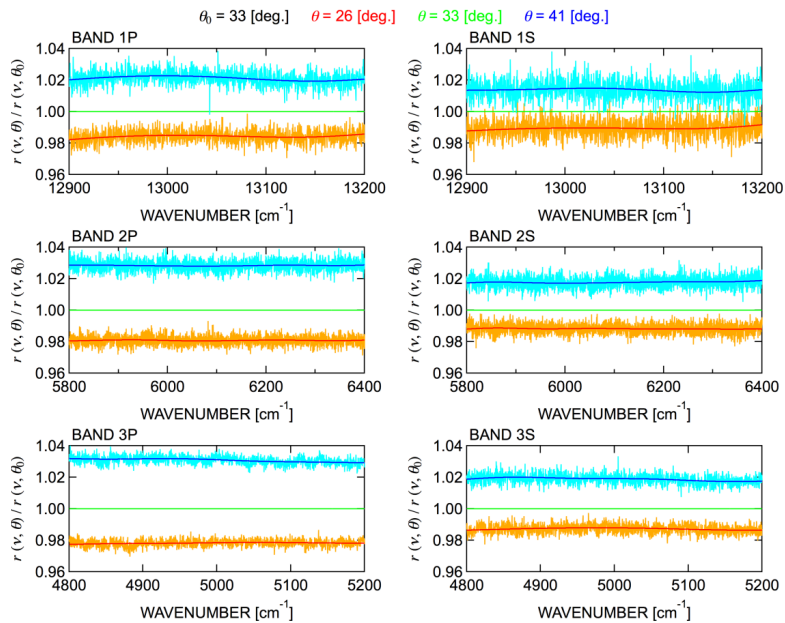
4730

$\theta_0 = 33$ [deg.] $\theta = 26$ [deg.] $\theta = 33$ [deg.] $\theta = 41$ [deg.]

Fig. 6. Incident angle dependency of the reflectance spectrum of the diffuser plate.

4731
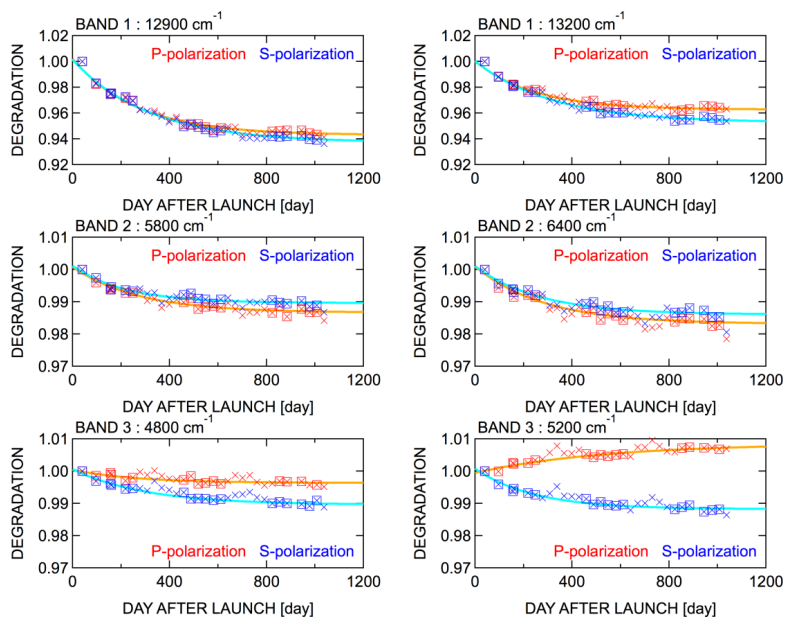
Fig. 7. Radiometric degradation of TANSO-FTS evaluated from the on-orbit solar calibration data (cross). For curve fitting, data observed with the incident angle less than 35 degree (square) were used.
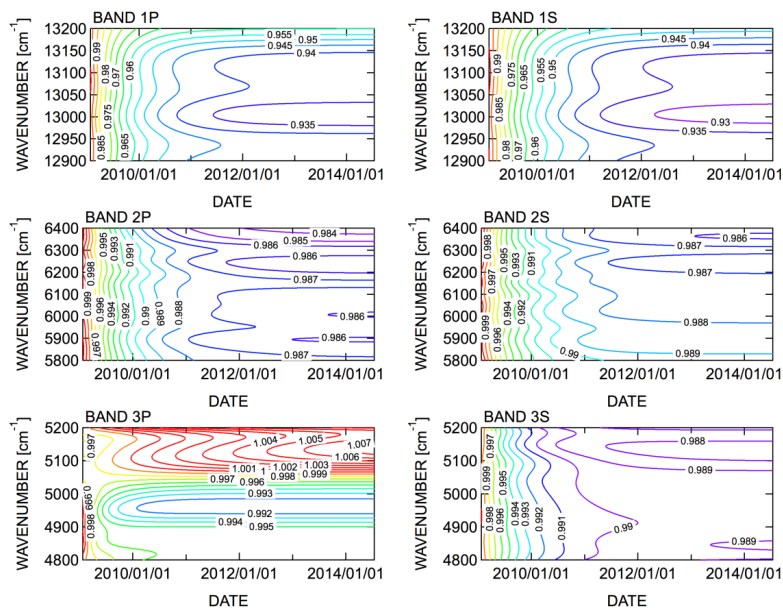
4732

Fig. 8. The TANSO-FTS radiometric degradation over 5.5 yr in various spectral bands calculated from the radiometric degradation model evaluated in this study.
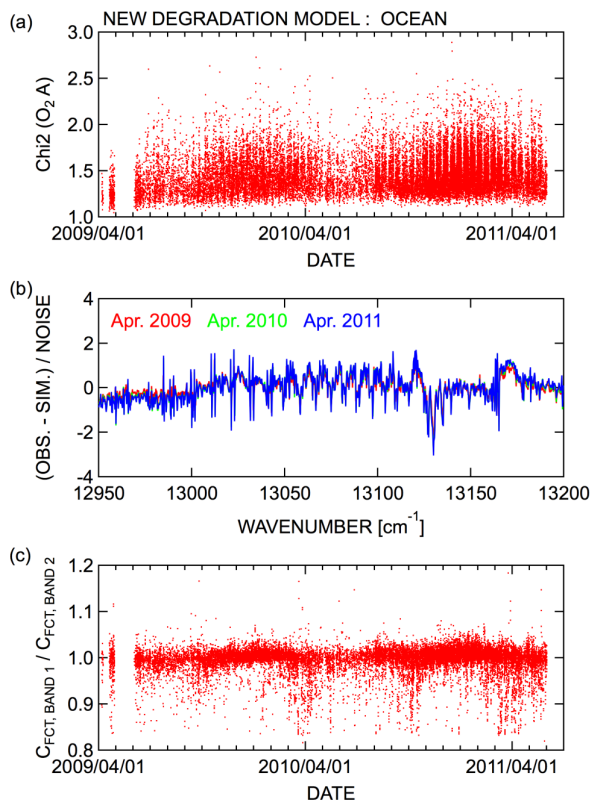
Fig. 9. Same as Fig. 2 except that the new degradation model evaluated in this study was used in this retrieval analysis.